Including higher order multipoles in gravitational-wave models for precessing binary black holes

Sebastian Khan,[1,2,3] Frank Ohme,[2,3] Katerina Chatziioannou,[4] and Mark Hannam[1,5]

[1]*School of Physics and Astronomy, Cardiff University, The Parade, Cardiff CF24 3AA, United Kingdom*
[2]*Max Planck Institute for Gravitational Physics (Albert Einstein Institute), Callinstr. 38, 30167 Hannover, Germany*
[3]*Leibniz Universität Hannover, D-30167 Hannover, Germany*
[4]*Center for Computational Astrophysics, Flatiron Institute, 162 5th Ave, New York, New York 10010, USA*
[5]*Dipartimento di Fisica, Università di Roma "Sapienza", Piazzale A. Moro 5, I-00185 Roma, Italy*

(Received 21 November 2019; published 30 January 2020)

Estimates of the source parameters of gravitational-wave (GW) events produced by compact binary mergers rely on theoretical models for the GW signal. We present the first frequency-domain model for the inspiral, merger, and ringdown of the GW signal from precessing binary black hole systems that also includes multipoles beyond the leading-order quadrupole. Our model, `PhenomPv3HM`, is a combination of the higher-multipole nonprecessing model `PhenomHM` and the spin-precessing model `PhenomPv3` that includes two-spin precession via a dynamical rotation of the GW multipoles. We validate the new model by comparing to a large set of precessing numerical-relativity simulations and find excellent agreement across the majority of the parameter space they cover. For mass ratios < 5 the mismatch improves, on average, from ∼6% to ∼2% compared to `PhenomPv3` when we include higher multipoles in the model. However, we find mismatches ∼8% for a mass-ratio-6 and highly spinning simulation. We quantify the statistical uncertainty in the recovery of binary parameters by applying standard Bayesian parameter estimation methods to simulated signals. We find that, while the primary black hole spin parameters should be measurable even at moderate signal-to-noise ratios (SNRs) ∼30, the secondary spin requires much larger SNRs ∼200. We also quantify the systematic uncertainty expected by recovering our simulated signals with different waveform models in which various physical effects—such as the inclusion of higher modes and/or precession—are omitted and find that even in the low-SNR case (∼17) the recovered parameters can be biased. Finally, as a first application of the new model we analyze the binary black hole event GW170729. We find larger values for the primary black hole mass of $58.25^{+11.73}_{-12.53}\ M_\odot$ (90% credible interval). The lower limit (∼46 $M_\odot$) is comparable to the proposed maximum black hole mass predicted by different stellar evolution models due to the pulsation pair-instability supernova (PPISN) mechanism. If we assume that the primary black hole in GW170729 formed through a PPISN, then out of the four PPISN models we consider only the model of Woosley [1] is consistent with our mass measurements at the 90% confidence level.

DOI: 10.1103/PhysRevD.101.024056

I. INTRODUCTION

The second-generation gravitational-wave (GW) detectors—Advanced LIGO [2] and Virgo [3]—have so far published observations of 11 compact binary mergers from the first two observing runs [4], including one binary neutron star merger that was also observed across the electromagnetic spectrum [5]. The third observing run is currently underway, with further sensitivity improvements planned in the coming years [6]. GW observations have already begun to constrain models of the formation and rates of stellar-mass compact binary mergers [7] and allowed for strong-field tests of the general theory of relativity [8].

Models for the GW signal, parametrized in terms of the properties of the system (such as masses, spins, and orientation), are compared with detector data to infer the source properties of GW events. The GW signal is commonly expressed in a multipole expansion where we denote terms beyond the leading-order quadrupole contribution as "higher-order multipoles." These higher-order multipoles are typically much weaker than the dominant quadrupolar multipole, but grow in relative strength for systems that are more asymmetric in mass. Past studies have shown that for events where the signal contains measurable power in the higher multipoles, parameter estimates can be biased when using only a dominant-multipole model. Conversely, it is also true that for some systems we are able to measure the source parameters more accurately using a higher-multipole model [9–14].

Another important physical effect is spin precession, where couplings between the orbital and spin angular

momenta can cause the orbital plane to precess and thus cause modulations of the observed GW [15,16]. In terms of the GW multipoles, precession mixes together different orders (m multipoles) of the same degree (ℓ multipoles), complicating a simple description of the waveform [17–24]. By not taking into account precession and higher-order multipoles in our waveform models we may not be able to confidently detect and accurately characterize signals where these effects are important [25–30]. These events are also likely to be very interesting astrophysically, providing valuable information about binary black hole (BBH) formation mechanisms and hence are events with high scientific gain that we wish to model and measure accurately.

The field of waveform modeling has seen sustained development over almost two decades and is currently thriving, with improvements to current methods and the development of novel methods allowing for more accurate and efficient models to be applied in data analysis pipelines [10,31–54]. In this work we take a step towards including as many important physical effects as possible in waveform models by constructing the most physically complete phenomenological model to date. We present a frequency-domain model for the GW signal from the inspiral, merger, and ringdown of a BBH system. The BHs are allowed to precess and we also model the contribution to the GW signal from higher-order multipoles. This combines the progress made in two earlier models: a precessing-binary model that includes accurate two-spin precession effects during the inspiral [55,56] (`PhenomPv3` [50]), and an approximate higher-multipole aligned-spin model (`PhenomHM` [10]).

Figure 1 demonstrates the improved accuracy that is achievable by our new model, `PhenomPv3HM`, compared to other existing models that include the effect of spin precession, but not higher-order multipoles. We compare the observed GW signal predicted by our new model against a high-mass-ratio, precessing numerical relativity (NR) simulation[1] (thick grey line). We plot the GW signal observed at an inclination angle[2] of $\pi/2$ rad to emphasize the effect of precession. We use all multipoles in the range $2 \leq \ell \leq 4$ when computing the NR GW polarizations.

We compute the mismatch (defined in Sec. III A) between three different precessing waveform models and the NR waveform, and average over all possible orientations. The top panel shows the optimal waveform (in blue) when we use `SEOBNRv3` [43] and the middle panel shows (in orange) the result when we use `PhenomPv3`. In this context the optimal waveform maximizes the overlap over coalescence time, template phase, and polarization angle,

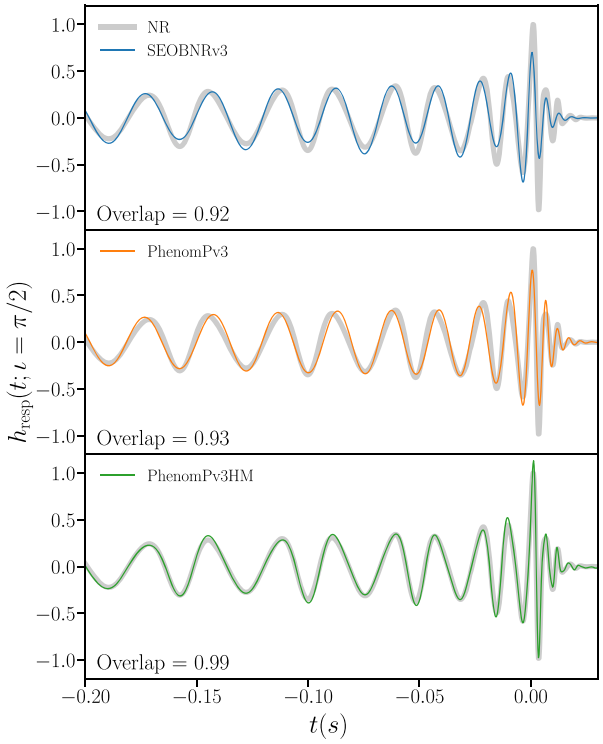

FIG. 1. Comparison of the detector response strain $h(t)$ viewed at an inclination angle of $\pi/2$. Solid grey: NR simulation (SXS:BBH:0058). We use a mass-ratio $q \equiv m_1/m_2 = 5$, precessing BBH simulation with a dimensionless-spin magnitude of $\chi_1 = 0.5$ generated with a total mass of 80 $M_\odot$. The NR signal contains all of the ℓ, m modes up to and including $\ell = 4$. Top panel, blue: Precessing model `SEOBNRv3` [58], with the $((2,\pm2), (2,\pm1))$ modes in the coprecessing frame. Middle panel, orange: Precessing model `PhenomPv3` [50] with only the $2,\pm2$ modes in the coprecessing frame. Bottom panel, green: Precessing model presented here, `PhenomPv3HM`, with the $(\ell,|m|) = ((2,2), (2,1), (3,3), (3,2), (4,4), (4,3))$ modes in the coprecessing frame. The orientation-averaged mismatch $1 - \bar{\mathcal{M}}$ (see Sec. III A) is 8% for the top panel, 7% for the middle panel, and 1% for the bottom panel. We only plot the last ∼7 GW cycles for clarity but the behavior is qualitatively the same throughout the 29-orbit inspiral (∼60 GW cycles).

and the intrinsic parameters are fixed to the values from the NR simulation. As shown in Ref. [50], `SEOBNRv3` and `PhenomPv3` have overlaps of ∼99% and ∼98%, respectively, to this NR waveform when only the $\ell = 2$ multipoles are considered. When we include higher-order multipoles in the NR waveform we find that the overlap drops to only ∼92% and ∼93%, respectively. This is an example where the exclusion of higher multipoles in template models can lead to unacceptable losses in signal-to-noise ratio (SNR). The bottom panel shows, in green, the best-fitting `PhenomPv3HM` template. We find remarkable agreement, even through the inspiral, merger, and ringdown stages. The overlap is now 99% and the subtle modulation visible is accurately captured by our model. It is useful to point out here that, in

[1]The NR waveform is SXS:BBH:0058 from the SXS public catalogue [57]. It has a mass ratio of $q = 5$ with spin on the larger BH directed in the orbital plane with a dimensionless spin magnitude of $\chi_1 = 0.5$.

[2]Here we define the inclination as the angle between the orbital angular momentum and the line of sight at the beginning of the waveform.

PhenomPv3HM, the higher multipole and the precession elements of the model have not been calibrated to NR simulations, but when this is done we expect the accuracy to improve further.

The rest of the paper is organized as follows. In Sec. II we describe how our model is constructed. In Sec. III A we compare our model against precessing NR simulations including higher-order multipoles up to and including $\ell = 4$ to demonstrate its accuracy across the parameter space where we have NR simulations. We also perform a parameter estimation study to quantify the impact on parameter recovery when using a model that includes both higher multipoles and precession, the results of which are presented in Sec. III B.

Finally, in Sec. III C we analyze data for the GW170729 event, publicly available at the Gravitational Wave Open Science Center [59], which has evidence for nonzero BH spin [4] and unequal masses [11].

II. METHOD

Our method to build a model for the GW signal from precessing BBHs is based upon the novel ideas of Refs. [18,23,60], where the GW from precessing binaries can be modeled as a dynamic rotation of nonprecessing systems. In Refs. [35,37,58] the authors used these ideas to build the first precessing inspiral-merger-ringdown (IMR) models.

Our goal is to derive frequency-domain expressions for the GW polarizations $\tilde{h}_{+/\times}(f)$ in terms of the multipoles $\tilde{h}_{\ell m}(f)$. We start from the complex GW quantity, $h = h_+ - ih_\times$, in the time domain and decompose this into spin weight -2 spherical harmonics,

$$h(t,\vec{\lambda},\theta,\phi) = \sum_{\ell\geq 2}\sum_{-\ell\leq m\leq\ell} h_{\ell,m}(t,\vec{\lambda})\,{}_{-2}Y_{\ell,m}(\theta,\phi). \quad (1)$$

This is a function of the time t, the intrinsic source parameters (masses and spin angular momenta of the bodies) denoted by $\vec{\lambda}$, and the polar angles θ and ϕ of a coordinate system whose z axis is aligned with the total angular momentum $\vec{J}$ of the binary at some reference frequency. To approximate the precessing multipoles $h^{\rm prec}_{\ell,m}(t)$ we perform a dynamic rotation of the nonprecessing multipoles $h^{\rm non\text{-}prec}_{\ell,m}(t)$,

$$h^{\rm prec}_{\ell,m}(t) = \sum_{-\ell\leq m'\leq\ell} h^{\rm non\text{-}prec}_{\ell,m'}(t) D^{\ell}_{m',m}(\alpha(t),\beta(t),\epsilon(t)). \quad (2)$$

We define the Wigner D matrix as $D^{\ell}_{m',m}(\alpha,\beta,\epsilon) = e^{im\alpha} d^{\ell}_{m',m}(-\beta) e^{-im'\epsilon}$ and the Wigner d matrix is given in Ref. [61].

Next we transform to the frequency domain using the stationary-phase approximation [62] under the assumption that the precession angles modify the signal via a slowly varying amplitude, giving us an expression for the frequency-domain multipoles in terms of the coprecessing frame multipoles,

$$\tilde{h}^{\rm prec}_{\ell,m}(f) = \sum_{-\leq\ell<m'\leq\ell} \tilde{h}^{\rm non\text{-}prec}_{\ell,m'}(f) D^{\ell}_{m',m}(\alpha,\beta,\epsilon). \quad (3)$$

For brevity we omit the explicit dependence on frequency for the precession angles (α, β, ϵ), but they are evaluated at the stationary points $t(f) = 2\pi f/m'$ [39].

The frequency-domain GW polarizations $\tilde{h}_{+/\times}(f)$ are defined as the Fourier transform (FT) of the real-valued GW polarizations $h_{+/\times}(t)$, which we write as

$$\tilde{h}_+(f) = \mathrm{FT}[\mathrm{Re}(h(t))] = \frac{1}{2}(\tilde{h}(f) + \tilde{h}^*(-f)), \quad (4)$$

$$\tilde{h}_\times(f) = \mathrm{FT}[\mathrm{Im}(h(t))] = \frac{i}{2}(\tilde{h}(f) - \tilde{h}^*(-f)). \quad (5)$$

To arrive at the final expression for the frequency-domain GW polarizations we substitute Eq. (3) into Eqs. (4) and (5), assuming $f > 0$ and symmetry through the orbital plane in the coprecessing frame,[3] leading to

$$\tilde{h}^{\rm prec}_+(f) = \frac{1}{2}\sum_{\ell\geq 2}\sum_{m'>0} \tilde{h}^{\rm non\text{-}prec}_{\ell,m'}(f) \sum_{m=-\ell}^{\ell} (A^{\ell}_{m',m} + (-1)^{\ell} A^{*\ell}_{-m',m}), \quad (6)$$

$$\tilde{h}^{\rm prec}_\times(f) = -\frac{i}{2}\sum_{\ell\geq 2}\sum_{m'>0} \tilde{h}^{\rm non\text{-}prec}_{\ell,m'}(f) \sum_{m=-\ell}^{\ell} (A^{\ell}_{m',m} - (-1)^{\ell} A^{*\ell}_{-m',m}). \quad (7)$$

To shorten the expression we define the auxiliary matrix $A^{\ell}_{m',m} \equiv {}_{-2}Y_{\ell,m} D^{\ell}_{m',m}$ and omit the explicit angular dependence of ${}_{-2}Y_{\ell,m}$ and the precession angles in $D^{\ell}_{m',m}$. The summation over ℓ and m' are over the modes included in the coprecessing frame. Here we use the PhenomHM model [10], which contains the $(\ell, |m'|) = ((2,2),(2,1),(3,3),(3,2),(4,4),(4,3))$ modes.

Due to precession the properties of the remnant BH in the precessing system are different to those in the equivalent nonprecessing system. We use the same prescription as described in Sec. III C of Ref. [50] to include the in-plane-spin contribution to the spin of the remnant BH. This modified final spin vector changes the ringdown spectrum of the aligned-spin multipoles.

Last, we note that the models for the three ingredients (the nonprecessing model, the precession angles, and the BH remnant model) are independent in our construction,

[3]This leads to the simplification $\tilde{h}_{\ell,m'}(f) = (-1)^{\ell}\tilde{h}^*_{\ell,-m'}(-f)$.

and can therefore each be updated when any of them are improved.

III. WAVEFORM ASSESSMENT

A. Mismatch computation

The standard metric to assess the accuracy of GW signal models is to calculate the noise-weighted inner product between the *template* model and an accurate *signal* waveform. As our signal we use NR waveforms from the publicly available SXS catalogue [57,63,64] generated using the NR injection infrastructure in LALSuite [65]. From this catalogue we select the precessing configurations with the highest numerical resolution. This set contains 90 systems with $q \in [1,6]$; however, the majority of cases have $q \leq 3$. We have two cases at $q = 5$ and one case at $q = 6$. There are six cases that have at least one BH with a dimensionless spin magnitude $|\chi| > 0.5$, whereas the majority of cases have $|\chi| \leq 0.5$.[4] For the exact list of NR configurations and specific details on how the mismatch calculations were performed we refer the reader to Ref. [50], where we presented an identical analysis but restricted the signals to contain the $\ell = 2$ multipoles.

Since `PhenomPv3` is constructed from `PhenomD` it only has the $\ell = |m| = 2$ modes in the coprecessing frame, and therefore we expect this model to perform poorly when the contribution to the signal due to higher modes is not negligible. As `PhenomPv3HM` is constructed from `PhenomHM` and contains the $(\ell, |m|) = ((2,2),(2,1),(3,3),(3,2),(4,4),(4,3))$ modes in the coprecessing frame, we expect it to outperform `PhenomPv3`. In the NR signal we include multipoles with $\ell \in [2,4]$ to be consistent with the highest modeled ℓ mode in `PhenomPv3HM`.

We use the expected noise curve for Advanced LIGO operating at design sensitivity [66][5] with a low-frequency cutoff of 10 Hz. Due to the presence of higher modes the orbital phase of the binary is no longer degenerate with the phase of the observed waveform, which means the standard method to analytically maximize over the template phase is not applicable. It is possible, however, to analytically maximize over the template polarization using the sky-maxed SNR derived in Ref. [28]. In our match calculation we analytically maximize over the template polarization and relative time shift and numerically optimize over the template orbital reference phase and frequency. Finally, we average the match, weighted by the optimal SNR, over the signal orbital reference phase and polarization angle. See Sec. III A in Ref. [50] for details.

[4]During the concluding stages of this project the SXS Collaboration updated their catalogue to include ~2000 new simulations [64]. We defer comparison to this catalogue to a future date.

[5]See Ref. [67] for a more recent reference.

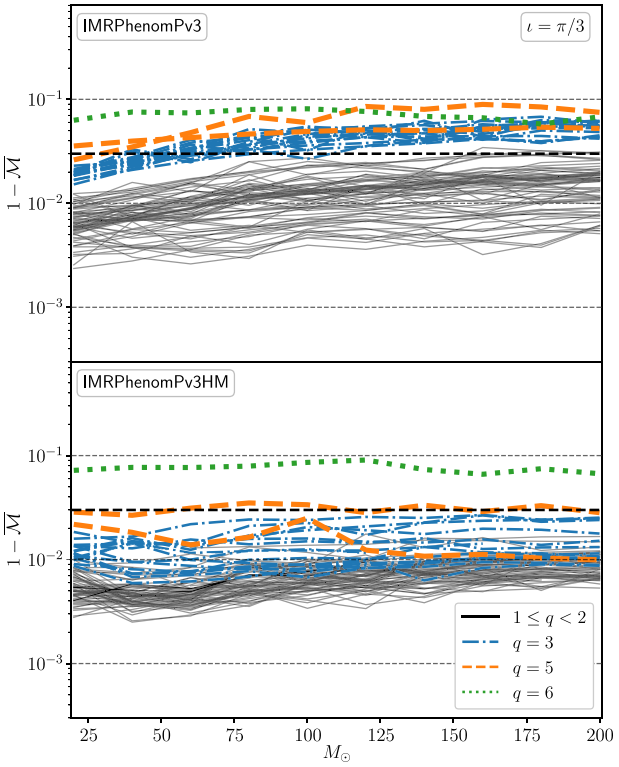

FIG. 2. The results of the comparison between `PhenomPv3` (top), `PhenomPv3HM` (bottom), and the precessing NR simulations from the public SXS catalogue. The figure shows the mismatch average over a reference phase and polarization angle $(1 - \bar{\mathcal{M}})$ as a function of the total mass for an inclination of $\iota = \pi/3$. The worst case is SXS:BBH:0165, a short (~6 orbits) signal with mass ratio of 1:6 and high precession.

Figure 2 shows the orientation-averaged mismatch [50] as a function of the total mass of the binary for an inclination angle $\iota = \pi/3$. Here ι is the angle between the Newtonian orbital angular momentum and the line of sight at the start frequency of the NR waveform. The first row uses the dominant multipole-only model, `PhenomPv3`, and the second row uses the new higher-multipole model, `PhenomPv3HM`, presented here. We clearly see that for $q \geq 3$ it is important to include higher modes in the template model.

In Table I we summarize the results of our validation study by tabulating the results as the match (as opposed to mismatch as in Fig. 2) for each model according to mass ratio and inclination angle. Next to the mass-ratio range in parentheses is the number of NR cases in that mass-ratio category. Each entry in the table is calculated as follows: for the $M_{\rm tot} = 100\,M_\odot$ case we average the match over all cases in the mass-ratio category and write the minimum and maximum match as a subscript and superscript, respectively.

$1 \leq q \leq 2$: In this mass-ratio range both `PhenomPv3` and `PhenomPv3HM` perform comparably, most likely due

TABLE I. Match results from Sec. III A. We quote the mean value of the match for each inclination angle considered ($\iota \in [0, \pi/3, \pi/2]$ rad) and averaged over all cases in the mass-ratio category for the $M_{\rm tot} = 100\ M_\odot$ case. The subscript and superscript are the minimum and maximum values of the match for the mass-ratio category considered.

Waveform Model	PhenomPv3			PhenomPv3HM		
Mass Ratio (#)	0	$\pi/3$	$\pi/2$	0	$\pi/3$	$\pi/2$
$1 \le q \le 2$ (72)	$0.998^{0.999}_{0.993}$	$0.989^{0.996}_{0.977}$	$0.982^{0.993}_{0.967}$	$0.997^{0.999}_{0.993}$	$0.993^{0.996}_{0.986}$	$0.987^{0.992}_{0.972}$
$q = 3$ (15)	$0.989^{0.999}_{0.974}$	$0.959^{0.967}_{0.950}$	$0.941^{0.946}_{0.933}$	$0.993^{0.997}_{0.985}$	$0.987^{0.993}_{0.975}$	$0.984^{0.989}_{0.974}$
$q = 5$ (2)	$0.973^{0.978}_{0.968}$	$0.941^{0.951}_{0.931}$	$0.911^{0.925}_{0.897}$	$0.990^{0.990}_{0.989}$	$0.971^{0.975}_{0.966}$	$0.978^{0.989}_{0.968}$
$q = 6$ (1)	0.863	0.919	0.939	0.950	0.914	0.898

to the strength of higher multipoles scaling with the mass ratio.

$q = 3$: Here we start to see the importance of the higher multipoles to accurately describe the NR signal. For $\iota = 0$, PhenomPv3 has an average match of 0.989. However, as the inclination angle increases, thus emphasizing more of the higher-multipole content of the signal, the average match drops to 0.941 and can be as low as 0.933. On the other hand, PhenomPv3HM is able to describe the NR data to an average accuracy of 0.984 with a minimum value of 0.974 for inclined systems.

$q = 5$: At this mass ratio the loss in performance for PhenomPv3 is noticeable even for low inclination values. At $\iota = 0$ the average match is 0.973, dropping to 0.911 at $\iota = \pi/2$. The match for PhenomPv3HM at $\iota = 0$ remains high at 0.99, but reduces to 0.978 at $\iota = \pi/2$. Note that we only have two NR simulations at $q = 5$ and are thus unable to rigorously test the model at this and similar mass ratios.

$q = 6$: When comparing to this NR simulation we find that both models perform substantially worse than the $q = 5$ cases, with even PhenomPv3 outperforming PhenomPv3HM with matches as low as 0.898. We have verified that we obtain matches of ∼0.97 when restricting the NR waveform to just the $\ell = 2$ multipoles, consistent with our previous study [50]. We conclude that either our model is outside its range of validity or that this NR simulation is inaccurate for the higher multipoles; however, our results are robust against NR simulations of this configuration at multiple resolutions. This NR simulation, SXS:BBH:0165, is exceptional for a few reasons. First, it is a high-mass-ratio system where higher multipoles are more important. Second, it is a strongly precessing system with primary $\chi_1 = (0.74, 0.19, -0.5)$ and secondary $\chi_2 = (-0.19, 0., -0.23)$ spin vectors. Finally, it is also very short, only containing ∼6.5 orbits. We encourage more NR simulations in this region by different NR codes to (i) cross-check the results and (ii) populate this region with more data with which to test and refine future models.

We conclude from our study that PhenomPv3HM greatly improves the accuracy for precessing BBHs for systems with mass ratios up to 5∶1. We expect to be able to greatly improve the accuracy and extend towards higher mass ratios by further calibrating the higher-order multipoles and precession effects to NR simulations.

B. Parameter uncertainty

One of the main purposes of a waveform model is to estimate the source parameters of GW events. With models we can quantify the expected parameter uncertainty as a function of the parameter space [68–76]. Instead of a computationally intense systematic parameter estimation campaign, we have chosen to focus on one configuration and study in detail the dependency of parameter recovery on SNR. We wish to study a system where both precession and higher modes are important and, guided by previous studies [25,26,77], we chose to study a double precessing spin, mass-ratio 3 BBH signal with a total mass of 150 $M_\odot$ in the detector frame. Starting at a frequency of 10 Hz, this system produces a waveform with about 20 GW cycles and merges at a frequency of about 120 Hz. See Table II for specific injection values, where (θ_{JN}, ϕ) define the direction of propagation in the source frame, (α, δ) are the right ascension and declination of the source, and ψ is the polarization angle.

We simulate this fiducial signal with PhenomPv3HM and recover its parameters using the parallel-tempered Markov chain Monte Carlo algorithm implemented as LALInferenceMCMC in the publicly available LALInference software [78] with PhenomPv3HM as the template model. We perform three separate, zero-noise injections to investigate how our results depend on the injected SNR. Specifically, we inject the signal at luminosity distances of 3000, 1500, and 300 Mpc, corresponding to a three-detector network SNR of 17, 35, and 176, respectively. We use the design sensitivity noise curves for the LIGO Hanford, LIGO Livingston, and Virgo detectors [66].

We present our results by tabulating the median and 90% credible interval on binary parameters in Table II and source-frame parameters in Table III. We also plot the 90%

TABLE II. Injection parameters and results from parameter estimation of simulated signals. We quote the median and 90% credible interval.

Parameter	Injection value	$\rho = 17.6$ $D_L = 3000$	$\rho = 35.2$ $D_L = 1500$	$\rho = 176$ $D_L = 300$
$m_1^{\rm det}/M_\odot$	112.500	$102.98^{+13.38}_{-12.26}$	$107.71^{+7.96}_{-7.43}$	$112.38^{+1.73}_{-1.75}$
$m_2^{\rm det}/M_\odot$	37.500	$40.62^{+5.92}_{-5.29}$	$39.00^{+2.88}_{-2.66}$	$37.55^{+0.54}_{-0.52}$
$M_{\rm total}^{\rm det}/M_\odot$	150.000	$143.64^{+11.28}_{-9.74}$	$146.78^{+6.48}_{-5.94}$	$149.93^{+1.49}_{-1.46}$
$\mathcal{M}_c^{\rm det}/M_\odot$	54.940	$55.08^{+3.37}_{-3.20}$	$55.05^{+1.69}_{-1.69}$	$54.95^{+0.36}_{-0.34}$
q	0.333	$0.39^{+0.11}_{-0.08}$	$0.36^{+0.05}_{-0.04}$	$0.33^{+0.01}_{-0.01}$
θ_1/ rad	1.052	$1.14^{+0.36}_{-0.37}$	$1.10^{+0.27}_{-0.19}$	$1.05^{+0.04}_{-0.04}$
θ_2/ rad	2.090	$1.73^{+1.01}_{-1.21}$	$2.04^{+0.72}_{-1.09}$	$2.09^{+0.14}_{-0.12}$
$\Delta\phi_{12}$/ rad	1.571	$2.82^{+3.11}_{-2.49}$	$1.79^{+3.42}_{-1.35}$	$1.58^{+0.24}_{-0.24}$
θ_{JN}/ rad	1.050	$1.62^{+0.60}_{-0.73}$	$1.21^{+0.92}_{-0.23}$	$1.05^{+0.03}_{-0.03}$
$\cos(\phi)$	1.000	$-0.04^{+1.03}_{-0.96}$	$0.46^{+0.54}_{-1.46}$	$1.00^{+0.00}_{-0.01}$
α/ rad	1.047	$4.235^{+0.124}_{-3.213}$	$1.070^{+3.277}_{-0.036}$	$1.047^{+0.004}_{-0.004}$
δ/ rad	1.047	$-1.020^{+2.098}_{-0.125}$	$1.025^{+0.037}_{-2.155}$	$1.047^{+0.004}_{-0.004}$
ψ/ rad	1.047	$1.52^{+0.66}_{-0.76}$	$1.28^{+0.80}_{-0.39}$	$1.05^{+0.04}_{-0.04}$
$\chi_{\rm eff}$	0.200	$0.204^{+0.129}_{-0.136}$	$0.201^{+0.070}_{-0.074}$	$0.200^{+0.016}_{-0.017}$
χ_p	0.700	$0.681^{+0.186}_{-0.285}$	$0.705^{+0.098}_{-0.105}$	$0.699^{+0.020}_{-0.024}$
$\lvert\chi_1\rvert$	0.806	$0.77^{+0.15}_{-0.27}$	$0.80^{+0.07}_{-0.09}$	$0.81^{+0.02}_{-0.02}$
$\lvert\chi_2\rvert$	0.806	$0.45^{+0.47}_{-0.40}$	$0.59^{+0.35}_{-0.42}$	$0.80^{+0.13}_{-0.11}$
D_L/Mpc	see heading	$3086.50^{+739.44}_{-571.98}$	$1465.76^{+177.84}_{-157.87}$	$300.12^{+7.14}_{-6.94}$

TABLE III. Source-frame injection parameters and results from parameter estimation of simulated signals. We quote the median and 90% credible interval.

	$\rho = 17$		$\rho = 34$		$\rho = 176$	
Parameter	Inj.	Rec.	Inj.	Rec.	Inj.	Rec.
$m_1^{\rm src}/M_\odot$	74.56	$67.60^{+8.22}_{-8.35}$	87.789	$84.28^{+5.36}_{-5.24}$	105.724	$105.54^{+1.55}_{-1.58}$
$m_2^{\rm src}/M_\odot$	24.853	$26.60^{+3.95}_{-3.55}$	29.263	$30.48^{+2.47}_{-2.21}$	35.241	$35.27^{+0.51}_{-0.50}$
$M_{\rm total}^{\rm src}/M_\odot$	99.413	$94.35^{+6.64}_{-7.16}$	117.052	$114.82^{+3.97}_{-3.96}$	140.965	$140.80^{+1.28}_{-1.27}$
$M_c^{\rm src}/M_\odot$	36.412	$36.11^{+2.29}_{-2.34}$	42.872	$43.04^{+1.31}_{-1.28}$	51.631	$51.61^{+0.31}_{-0.30}$
D_L/Mpc	3000	$3086.50^{+739.44}_{-571.98}$	1500	$1465.76^{+177.84}_{-157.87}$	300	$300.12^{+7.14}_{-6.94}$
z	0.509	$0.52^{+0.10}_{-0.08}$	0.281	$0.28^{+0.03}_{-0.03}$	0.064	$0.065^{+0.001}_{-0.001}$

credible interval as a function of the injected SNR for a few chosen parameters in Figs. 3, 4, and 5. In the high-SNR limit the uncertainty on the parameters should decrease linearly with SNR, i.e., as $1/\rho$ [79], which is shown as a dashed black line in these figures.

In the following discussion we change our convention for the mass ratio to $q \equiv m_2/m_1 \in [0, 1]$ and will abbreviate the width of the 90% credible interval of parameter X at a SNR of ρ as $C^{\rho}_{90\%}(X)$.

1. Masses

Figure 3 shows the source-frame mass parameters: the primary mass $m_1^{\rm src}$, secondary mass $m_2^{\rm src}$, chirp mass $\mathcal{M}_c^{\rm src}$, total mass $M_{\rm total}^{\rm src}$, and mass ratio q. We find good scaling with respect to $1/\rho$ for all source-frame mass parameters.

Table III shows the injection and recovered values. Even at the high total masses we consider here we find that the chirp mass is still the best-measured parameter with $C^{17}_{90\%}(\mathcal{M}_c^{\rm src}) = 4.63\ M_\odot$ and $C^{176}_{90\%}(\mathcal{M}_c^{\rm src}) = 0.61\ M_\odot$. The total mass is the next-best-measured mass parameter with low- and high-SNR accuracies of $C^{17}_{90\%}(M_{\rm total}^{\rm src}) = 13.8\ M_\odot$ and $C^{176}_{90\%}(M_{\rm total}^{\rm src}) = 2.55\ M_\odot$, respectively. We find that the primary mass can be measured to an accuracy of $C^{17}_{90\%}(m_1^{\rm src}) = 16.57\ M_\odot$ for low SNR and $C^{176}_{90\%}(m_1^{\rm src}) = 3.13\ M_\odot$ for high SNR. For the secondary mass we find

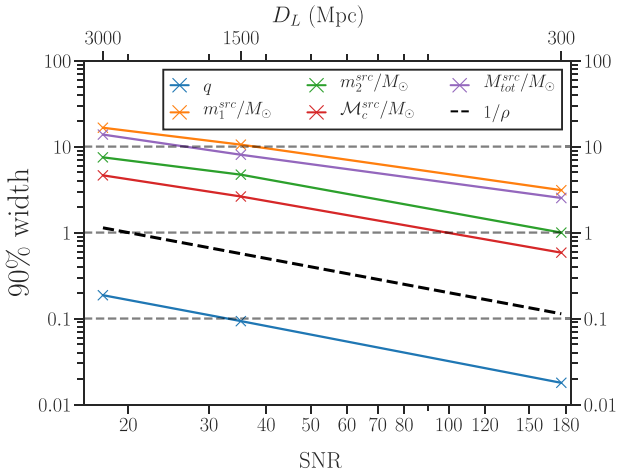

FIG. 3. 90% credible intervals for the source-frame mass parameters as a function of injected SNR.

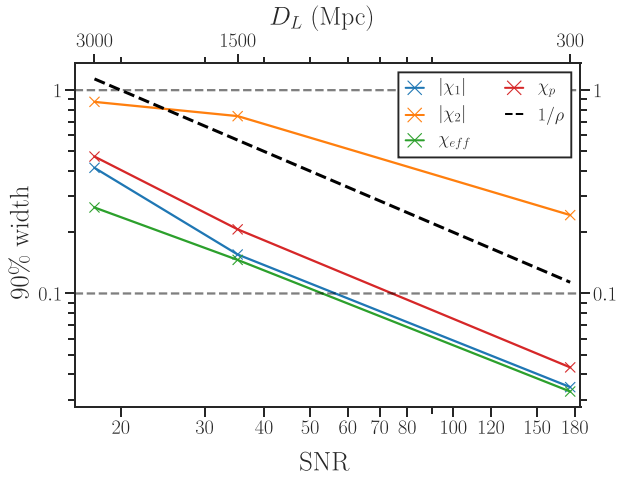

FIG. 4. 90% credible intervals for the BH spin magnitudes and effective spin parameters as a function of injected SNR.

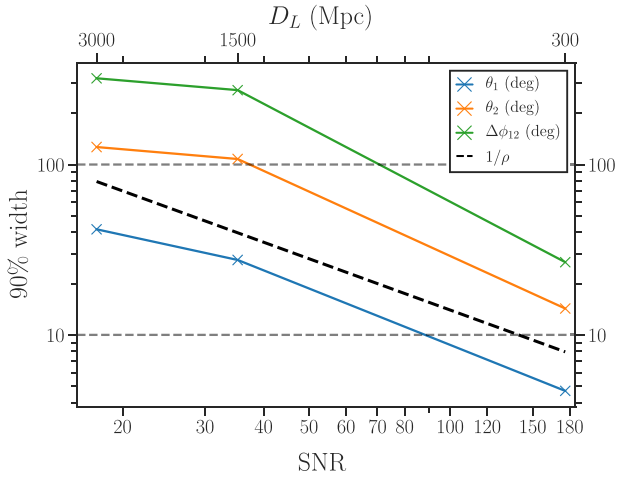

FIG. 5. 90% credible intervals for the BH spin orientation parameters as a function of injected SNR.

$C_{90\%}^{17}(m_2^{\rm src}) = 7.5\ M_\odot$ and $C_{90\%}^{176}(m_2^{\rm src}) = 1.01\ M_\odot$ for low and high SNR, respectively. Finally, we are able to constrain the mass ratio to $C_{90\%}^{17}(q) = 0.19$ and $C_{90\%}^{176}(q) = 0.02$.

2. Spins

Figure 4 shows the primary and secondary spin magnitude $|\chi_1|, |\chi_2|$, the effective aligned-spin $\chi_{\rm eff}$, and the effective precessing-spin $\chi_{\rm p}$ parameters.

With the exception of $|\chi_2|$ we find good agreement with the $1/\rho$ scaling. This suggests that for $|\chi_2|$ the two weaker injections do not have high enough SNRs for the posterior distribution function for this parameter to be approximated by a Gaussian [79]. That being said, we do observe the 90% width decrease with SNR, albeit at a slower rate. At SNRs of 17 and 34 we find that we are not able to place strong constraints on $|\chi_2|$ with $C_{90\%}^{17}(|\chi_2|) = 0.87$ and $C_{90\%}^{34}(|\chi_2|) = 0.77$. However, at the high SNR of 176 we begin to constrain the spin magnitude at the level of $C_{90\%}^{176}(|\chi_2|) = 0.24$, approximately the same level of uncertainty as $\chi_{\rm eff}$ at a SNR of 17. This is consistent with the study of nonprecessing binaries in Ref. [80], which concluded that the secondary spin will not be measurable for SNRs below ~100, but our results suggest that this carries over to precessing systems.

The primary spin magnitude is measured with much higher precision than the secondary spin magnitude. However, constraining this parameter to a 90% width of less than 0.2 requires a SNR of ~30. This parameter does follow the $1/\rho$ scaling very well and for high-SNR cases we estimate the statistical uncertainty to be $C_{90\%}^{176}(|\chi_1|) = 0.04$.

Of the effective spin parameters the effective aligned parameter $\chi_{\rm eff}$ is the best-measured quantity. This is closely related to the leading-order spin effect in post-Newtonian (PN) theory [81,82] appearing at 1.5PN order. For all three SNRs the median value is always within 10^{-3} of the true value, with the uncertainties ranging from $C_{90\%}^{17}(\chi_{\rm eff}) = 0.265$ to $C_{90\%}^{176}(\chi_{\rm eff}) = 0.033$.

Turning towards the effective precession spin parameter χ_p, at the lowest SNR we find that the marginalized posterior for χ_p has a median value of 0.681, close to the true value but with a wide uncertainty of $C_{90\%}^{17}(\chi_p) = 0.47$, spanning almost half of the full range. The evolution of the median value does not change significantly with increasing SNR; however, our measurement uncertainty does decrease with increasing SNR, as expected, and we find $C_{90\%}^{35}(\chi_p) = 0.203$ for the medium-SNR case and $C_{90\%}^{176}(\chi_p) = 0.044$ for the high-SNR case.

Figure 5 shows the spin orientation parameters. θ_1 and θ_2 are the polar angles of the primary and secondary spin vectors with respect to the orbital angular momentum at the reference frequency. The angle $\Delta\phi_{12}$ is the angle between the primary and secondary spin vectors projected onto the instantaneous orbital plane at the reference frequency.

TABLE IV. Waveform models that we use to analyze GW170729, highlighting which physical effects are included for each model.

Model	Precession	Higher modes
`PhenomD` [40,84]	✗	✗
`PhenomPv2` [37,85]	✓	✗
`PhenomPv3` [50]	✓	✗
`PhenomHM` [10]	✗	✓
`PhenomPv3HM`	✓	✓

This angle is particularly useful when characterizing precessing binaries as $\Delta\phi_{12} = 0$ or $\Delta\phi_{12} = \pi$ are resonant spin configurations (if other conditions on the mass-ratio and spin magnitudes are met) [83].

We find that θ_1 has good SNR scaling with $C^{17}_{90\%}(\theta_1) = 0.73$ rad (∼42 deg) and $C^{176}_{90\%}(\theta_1) = 0.08$ rad (∼5 deg). Furthermore, θ_2 and $\Delta\phi_{12}$ are measured much less accurately and require SNRs of ∼60 and ∼100 to achieve statistical uncertainties of ∼1 rad (∼60 deg), respectively. However, in the event of a high-SNR signal we that find we are able to constrain θ_2 to $C^{176}_{90\%}(\theta_2) = 0.26$ rad (∼15 deg) and $\Delta\phi_{12}$ to $C^{176}_{90\%}(\Delta\phi_{12}) = 0.48$ rad (∼28 deg).

In summary, we find that the primary spin magnitude $|\chi_1|$ and polar angle θ_1 can be constrained at a SNR of ∼30, while the secondary spin magnitude $|\chi_2|$ and polar angle θ_2 as well as the information about the relative orientation of the spin vectors $\Delta\phi_{12}$ are not constrained until we reach a SNR of ∼200.

3. Waveform systematics

Parameter estimation on a GW event with a waveform model that does not include relevant physics effects could result in biased results. To quantify the size of the bias due to neglecting higher modes and/or precession for this signal we repeat our parameter estimation analysis with four additional models.

The waveform models we use are listed in Table IV, where we mark whether or not each model contains precession and/or higher modes. `PhenomD` is the baseline model upon which the other `Phenom` models used in this work are built. We include two different precessing models —`PhenomPv2` and `PhenomPv3`—to gauge systematics on precession. `PhenomHM` includes higher modes but is a nonprecessing model, and finally we include the precessing and higher-mode model `PhenomPv3HM` presented in this article.

Our results are presented in Fig. 6. From left to right the columns show the one-dimensional marginalized posterior distributions for $m_1^{\rm det}$, $m_2^{\rm det}$, $\chi_{\rm eff}$, and $\chi_{\rm p}$. The rows from top to bottom show the results for the low ($\rho = 17$), medium ($\rho = 34$), and high ($\rho = 176$) SNR injections. The true value is shown as a vertical dashed black line. For all SNRs we find biases in the recovered masses for all models other than `PhenomPv3HM`, i.e., the model that was used to produce the synthetic signal. This suggests that real GW signals that are similar to this injection require analysis with models that contain *both* the effects of precession and higher modes. For the high-SNR case, multimode posteriors are found for the `PhenomD` case. For $\chi_{\rm eff}$ we find that for the low-SNR injection the true value is within the 90% credible interval (CI) and therefore not considered biased; however, as the SNR of the injection is increased we find that $\chi_{\rm eff}$ can become heavily biased for the two precessing models but remains unbiased for the nonprecessing models. For $\chi_{\rm p}$ we find that the precessing and non-higher-mode models (`PhenomPv2` and `PhenomPv3`) consistently

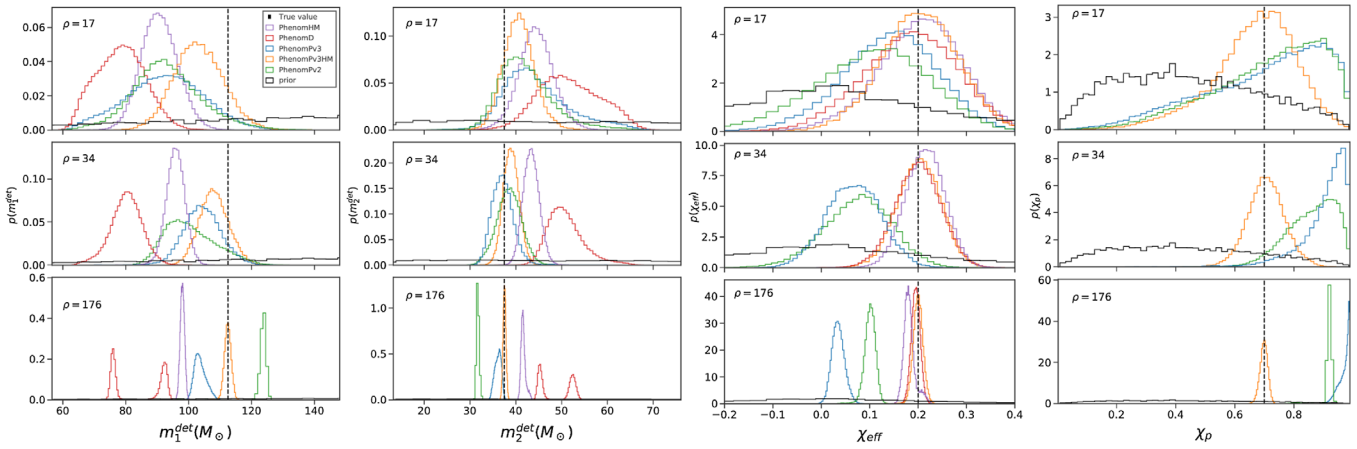

FIG. 6. One-dimensional marginal posterior probability distributions for detector-frame primary and secondary masses (first and second columns, respectively), effective aligned-spin $\chi_{\rm eff}$, and effective precession spin $\chi_{\rm p}$ parameters (third and fourth columns, respectively). Each row, from top to bottom, shows results for the low ($\rho = 17$), medium ($\rho = 34$), and high ($\rho = 176$) SNR injections. The true value is marked as a vertical black dashed line. The prior is shown as a black histogram. We show results for `PhenomD` (red), `PhenomHM` (purple), `PhenomPv2` (green), `PhenomPv3` (blue), and `PhenomPv3HM` (orange). Note that the results for $\chi_{\rm p}$ do not show `PhenomD` or `PhenomHM` as they are aligned-spin models only.

favor larger values of $\chi_{\rm p}$ as the SNR increases. Interestingly, we also start to find large differences between PhenomPv2 and PhenomPv3 in the high-SNR cases.

C. GW170729 analysis

Of the ten binary black hole observations reported by the LIGO/Virgo Collaboration [4], GW170729 shows the strongest evidence for unequal masses, making it the most likely signal for which higher modes could impact parameter measurements. This motivated the study in Ref. [11], where the authors analyzed GW170729 with two new aligned-spin and higher-mode models (SEOBNRv4HM [41] and PhenomHM [10]). They found that the models preferred to interpret the data as the GW signal coming from a higher-mass-ratio system, with estimates for the mass ratio changing from $0.62^{+0.36}_{-0.23}$ for PhenomPv2 to $0.52^{+0.26}_{-0.21}$ for PhenomHM (90% credible interval). This event also has evidence for a positive $\chi_{\rm eff}$, although when analyzed with higher modes the 90% credible interval for $\chi_{\rm eff}$ extended to include zero. This event was also analyzed in Ref. [86] with the aligned-spin and higher-mode model NRHybSur3dq8 [47], where the authors drew similar conclusions. Motivated by this, we prioritize GW170729 to analyze first with PhenomPv3HM and compare to existing results. We use the posterior samples for PhenomHM from Ref. [11] and for PhenomPv2 from Ref. [87]. Results for PhenomD, PhenomPv3, and PhenomPv3HM were computed for this work using the LALInferenceMCMC code [88].

In Fig. 7 we show the joint posterior for the source-frame component masses ($m_1^{\rm src}$, $m_2^{\rm src}$) in the upper left panel, the aligned effective spin and mass ratio ($\chi_{\rm eff}$, q) in the upper right panel, and finally the luminosity distance and inclination angle (D_L, ι) in the bottom panel. The quantitative parameter estimates for the source properties are provided in Table V. Our posterior on the effective precession

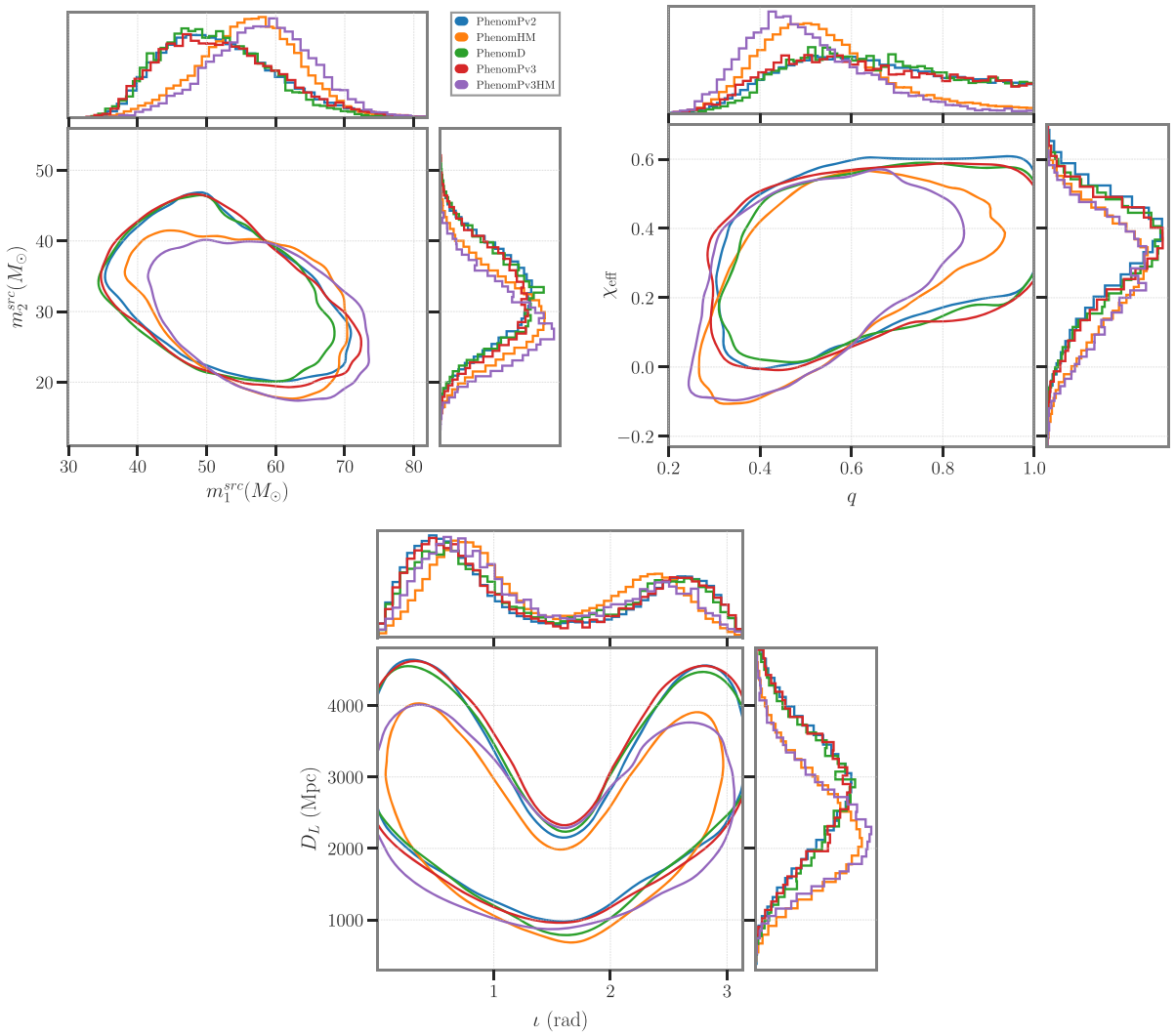

FIG. 7. GW170729 parameter estimation results. Top left: Component source-frame masses ($m_1^{\rm src}$, $m_2^{\rm src}$). Top right: Effective spin and mass ratio ($\chi_{\rm eff}$, q). Bottom: Inclination angle and luminosity distance (ι, D_L). The contour lines correspond to a credible level of 90%.

TABLE V. Parameter estimation results for GW170729. Masses are quoted in the source frame. We quote the median and the 90% symmetric credible interval of the one-dimensional marginalized posterior distributions.

Parameter	PhenomD	PhenomHM	PhenomPv2	PhenomPv3	PhenomPv3HM
Primary source mass: $m_1^{\rm src}/M_\odot$	$50.55^{+14.02}_{-10.64}$	$56.36^{+11.08}_{-12.41}$	$51.22^{+16.19}_{-10.99}$	$51.39^{+16.35}_{-11.58}$	$58.25^{+11.73}_{-12.53}$
Secondary source mass: $m_2^{\rm src}/M_\odot$	$32.18^{+10.18}_{-8.84}$	$29.45^{+9.72}_{-8.36}$	$32.43^{+9.75}_{-9.46}$	$31.67^{+10.43}_{-9.27}$	$28.18^{+9.83}_{-7.65}$
Total source mass: $M_{\rm total}^{\rm src}/M_\odot$	$82.80^{+15.29}_{-10.82}$	$85.16^{+14.00}_{-10.53}$	$83.93^{+14.74}_{-10.91}$	$83.52^{+14.94}_{-11.09}$	$86.18^{+13.42}_{-10.77}$
Mass ratio: q	$0.64^{+0.31}_{-0.24}$	$0.52^{+0.31}_{-0.18}$	$0.63^{+0.32}_{-0.26}$	$0.62^{+0.33}_{-0.26}$	$0.48^{+0.28}_{-0.16}$
Effective aligned spin: $\chi_{\rm eff}$	$0.34^{+0.19}_{-0.26}$	$0.28^{+0.22}_{-0.28}$	$0.36^{+0.19}_{-0.28}$	$0.34^{+0.19}_{-0.27}$	$0.27^{+0.21}_{-0.28}$
Effective precession spin: $\chi_{\rm p}$	N/A	N/A	$0.44^{+0.35}_{-0.29}$	$0.44^{+0.36}_{-0.30}$	$0.42^{+0.39}_{-0.29}$
Luminosity distance: D_L/MPc	2749^{+1353}_{-1359}	2241^{+1391}_{-1065}	2831^{+1371}_{-1340}	2797^{+1386}_{-1318}	2270^{+1307}_{-974}
Redshift: z	$0.48^{+0.19}_{-0.21}$	$0.40^{+0.20}_{-0.17}$	$0.49^{+0.19}_{-0.21}$	$0.48^{+0.19}_{-0.20}$	$0.41^{+0.19}_{-0.16}$

parameter χ_p is consistent with previous results and shows no significant differences due to a different choice of precession model (between PhenomPv2 and PhenomPv3) or including both precession and higher modes as in PhenomPv3HM. We find that the marginal posterior effective aligned-spin parameter $\chi_{\rm eff}$ and luminosity distance D_L are remarkably similar to the results from PhenomHM. The posterior for the inclination angle ι for IMPhenomPv3HM has more support for more inclined viewing angles; however, the change is minor.

Interestingly, we find remarkably consistent results between not only PhenomD and PhenomPv2 as discussed in Ref. [11], but also with PhenomPv3. This indicates that precession alone does not influence our inference for this event. However, including precession in addition to higher modes in the analysis does noticeably shift the posterior, albeit not very significantly in terms of the 90% CIs, which mostly overlap.

We find that the one-dimensional marginal posterior for the mass ratio is pushed further towards lower mass-ratio values (more asymmetric) when using PhenomPv3HM, where we find $q = 0.47^{+0.28}_{-0.16}$ (90% confidence level), implying that including precession *and* higher modes reinforces the findings of Ref. [11]. As more asymmetric masses are favored, the estimate for the primary mass (source frame) is shifted towards higher values and the secondary mass is shifted towards lower values, where we find $m_1^{\rm src} = 58.25^{+11.73}_{-12.53}\ M_\odot$ and $m_2^{\rm src} = 28.18^{+9.83}_{-7.65}\ M_\odot$.

By favoring larger mass estimates for the primary BH we challenge formation models to describe this event through standard stellar evolution mechanisms. In particular, our results inform the pulsational pair-instability supernova (PPISN) mechanism [1,89]. The population synthesis analysis in Ref. [90] investigated the resulting distribution of BH masses subject to different PPISN models. They found that in three out of the four models that they explored, the maximum BH mass is $\sim 40\ M_\odot$ [91–93], and in one of the models the maximum BH mass is $\sim 58\ M_\odot$ [1]. In Fig. 8 we show the one-dimensional marginal posterior for the source-frame primary mass resulting from the analysis using PhenomPv2 (blue), PhenomHM (orange), and PhenomPv3HM (purple). The 90% credible interval of each result is shown as the shaded area under their respective curves. The vertical black dashed lines denote the maximum BH mass from the four different PPISN models that were investigated in Ref. [90]. We do not show the posterior for PhenomD or PhenomPv3 as these are consistent with the PhenomPv2 posterior.

When using PhenomPv2 to analyze the data we find that the maximum BH masses for all PPISN models are consistent with the posterior. When we include nonprecessing, higher modes (PhenomHM) the PPISN models that

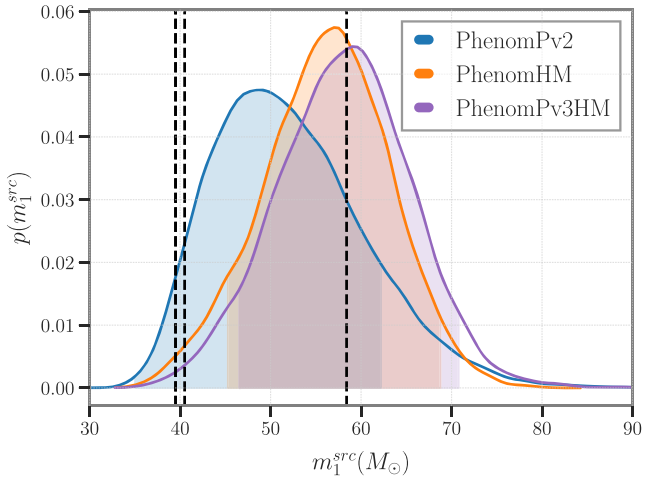

FIG. 8. One-dimensional marginal posterior distribution for the primary source-frame mass. The posteriors for the three waveform models are shown: PhenomPv2 (blue), PhenomHM (orange), and PhenomPv3HM (purple). The 90% credible interval of each result is shown as the shaded area under their respective curves. We also plot as vertical black dashed lines the maximum BH mass from four different PPISN models, which were investigated in Ref. [90]. Reference [1] predicted a maximum mass of 58.4 $M_\odot$, Ref. [91] predicted 40.5 $M_\odot$, and Refs. [92,93] both predicted 39.5 $M_\odot$.

predict maximum BH masses of $\sim 40\ M_\odot$ [91–93] are excluded at the following level. In the posterior, 1.3% of samples have a mass of $\leq 40\ M_\odot$. As noted previously, when we include both precession and higher modes the primary mass shifts slightly higher, resulting in 0.6% of samples having a mass of $\leq 40\ M_\odot$. If we assume that the primary BH in the GW170729 binary underwent a PPISN, then the following PPISN models [91–93] are disfavored at greater than 90% credibility and the maximum BH mass as predicted by Ref. [1] is consistent with our results. There are some caveats to these results, however. In Ref. [90] the authors used a linear fit to the PPISN model of Ref. [1] that systematically predicted larger remnant BH masses for pre-supernova helium (core) masses $M_{\rm He} > 60\ M_\odot$ than the model of Ref. [1] predicts. This in turn leads to larger maximum BH masses for this particular model. However, the size of this systematic uncertainty is unknown. Another caveat in the analysis of Ref. [90] is that the models [92,93] have an uncertainty of $\sim 5\ M_\odot$ to account for the difference between the gravitational and baryonic masses [94].

IV. DISCUSSION AND FUTURE

In this work we have presented the first, frequency-domain, phenomenological IMR model for spin-precessing BBHs that also includes the effects of subdominant multipoles—beyond the quadrupole—in the coprecessing frame. By comparing to a large set of precessing NR simulations we found that our simple model is able to accurately reproduce the expected GW signal with an accuracy of 99% (97%) for small (high) inclinations, a significant improvement over models that do not include subdominant multipoles, which have accuracies of 97% (91%) for small (high) inclinations.

Precise measurements of BH spins from GW observations requires high-SNR events, in part due to the relatively high PN order at which spin effects appear. We performed an idealized parameter estimation analysis to quantify the precision to which the BH spin magnitude and orientation can be measured, ignoring any effects of systematic error on the waveform. We found, for this particular system (see Table II), that the primary spin parameters are more tightly constrained than the secondary spin, as expected for an unequal-mass system such as this. In the following discussion we remind the reader that the low-, medium-, and high-SNR cases have corresponding values of 17, 34, and 176, respectively. The primary spin magnitude can be constrained to a 90% CI of 0.42 for the low-SNR case (about half the width of the physical range) and to a 90% CI of 0.04 for the high-SNR case. The secondary spin magnitude cannot be meaningfully constrained until the high-SNR case, with a 90% CI of 0.24. The primary spin polar angle shows reasonably good agreement with the expected SNR scaling and can be constrained to ~ 42 deg (low SNR) and ~ 5 deg (high SNR) at 90% CI. The secondary spin polar angle shows poor agreement with the expected SNR scaling and we find that it can only be meaningfully constrained (~ 15 deg) for the high-SNR case. The azimuthal angle between the spins ($\Delta\phi_{12}$) shows poor scaling with SNR. We find that only the highest SNR case was able to constrain $\Delta\phi_{12} \lesssim 28$ deg. Our parameter estimation study is only a point estimate for the size of the uncertainty on binary properties and a systematic study that explores the parameter space of precessing binaries is required to draw more general conclusions [68,69]. However, recent work in understanding precession better may help make such a study tractable by focusing on regions where we expect precession to be measurable [95,96].

We have analyzed the GW event GW170729 with the new precessing and higher-mode model. We have shown that while the general interpretation of this event is unchanged, we find that even small shifts in the posteriors due to using different waveform models, with different physical effects incorporated, can be enough to inform astrophysical models such as the PPISN mechanism, as we considered in this paper. If we assume that the primary BH in the GW170729 binary underwent a PPISN, then we disfavor the PPISN models from Refs. [91–93] at greater than 90% credibility and our results are consistent with Ref. [1]. See Ref. [97] for a recent investigation into the location of the PPISN model mass gap.

Our model is analytic and native to the frequency domain, and as such it can be readily used in likelihood acceleration methods such as reduced-order quadrature [98] or "multibanding" techniques [99]. This model can be used to determine the impact on GW searches, event parameter estimation, and population inference due to the effects of precession and higher modes.

We expect to be able to greatly improve `PhenomPv3HM` and similar models by using models for the underlying higher-multipole aligned-spin model that have been calibrated to NR waveforms [100]. Likewise, a model for the precession dynamics tuned to precessing NR simulations will improve its performance [101]. Although our model is a function of the seven-dimensional intrinsic parameter space of noneccentric BBH mergers, it is not seven-dimensional across the entire coalescence. It is true during the inspiral, but during the pre-merger and merger we use an effective aligned-spin parametrization. Work is underway to develop an NR -calibrated aligned-spin model with the effects of two independent aligned spins [102]. In addition, promising attempts to dynamically enhance incomplete models via singular-value decomposition have recently been presented [49], and the model introduced here can easily be employed by such an automated tuning process.

With regards to higher modes, we only included a subset of the complete list of modes, specifically, $(\ell, |m|) = ((2,2),(2,1),(3,3),(3,2),(4,4),(4,3))$. We also ignored mode mixing [103] and the asymmetry between the

$+m$ and $-m$ modes, which are responsible for out-of-plane recoils [104].

We plan to extend this model to include tidal effects, as introduced in Refs. [105,106], as well as implement a model for the GW suitable for neutron star–black hole binaries where the effects of spin precession, subdominant multipoles, and tidal effects could all become important. The model presented here could be used as a baseline for such a model. Finally, this model is implemented in the LSC Algorithm Library [107].

ACKNOWLEDGMENTS

We thank Geoffrey Lovelace, Lawrence Kidder, and Michael Boyle for support with the SXS catalogue. We thank Carl J. Haster and Yoshinta Setyawati for useful discussions. S. K. and F. O. acknowledge support by the Max Planck Society's Independent Research Group Grant. S. K. was also supported by European Research Council Consolidator Grant 647839. The Flatiron Institute is supported by the Simons Foundation. M. H. was supported by Science and Technology Facilities Council (STFC) Grant No. ST/L000962/1 and European Research Council Consolidator Grant 647839, and thanks the Amaldi Research Center for hospitality. We thank the Atlas cluster computing team at AEI Hannover. The authors are grateful for computational resources provided by the LIGO Laboratory and supported by National Science Foundation Grant Nos. PHY-0757058 and PHY-0823459. This work made use of numerous open source computational packages, such as PYTHON [108], NumPy, SciPy [109], Matplotlib [110], the GW data analysis software library PyCBC [111], and the LSC Algorithm Library [107]. This research has made use of data, software, and/or web tools obtained from the Gravitational Wave Open Science Center (https://www.gw-openscience.org), a service of LIGO Laboratory, the LIGO Scientific Collaboration, and the Virgo Collaboration. LIGO is funded by the U.S. National Science Foundation. Virgo is funded by the French Centre National de Recherche Scientifique (CNRS), the Italian Istituto Nazionale della Fisica Nucleare (INFN), and the Dutch Nikhef, with contributions from Polish and Hungarian institutes.

[1] S. E. Woosley, Astrophys. J. **836**, 244 (2017).
[2] J. Aasi *et al.* (LIGO Scientific Collaboration), Classical Quantum Gravity **32**, 074001 (2015).
[3] F. Acernese *et al.* (Virgo Collaboration), Classical Quantum Gravity **32**, 024001 (2015).
[4] B. P. Abbott *et al.* (LIGO Scientific and Virgo Collaborations), arXiv:1811.12907.
[5] B. P. Abbott *et al.* (GROND, SALT Group, OzGrav, DFN, INTEGRAL, Virgo, Insight-Hxmt, MAXI Team, Fermi-LAT, J-GEM, RATIR, IceCube, CAASTRO, LWA, ePESSTO, GRAWITA, RIMAS, SKA South Africa/MeerKAT, H.E.S.S., 1M2H Team, IKI-GW Follow-up, Fermi GBM, Pi of Sky, DWF (Deeper Wider Faster Program), Dark Energy Survey, MASTER, AstroSat Cadmium Zinc Telluride Imager Team, Swift, Pierre Auger, ASKAP, VINROUGE, JAGWAR, Chandra Team at McGill University, TTU-NRAO, GROWTH, AGILE Team, MWA, ATCA, AST3, TOROS, Pan-STARRS, NuSTAR, ATLAS Telescopes, BOOTES, CaltechNRAO, LIGO Scientific, High Time Resolution Universe Survey, Nordic Optical Telescope, Las Cumbres Observatory Group, TZAC Consortium, LOFAR, IPN, DLT40, Texas Tech University, HAWC, ANTARES, KU, Dark Energy Camera GW-EM, CALET, Euro VLBI Team, ALMA Collaborations), Astrophys. J. **848**, L12 (2017).
[6] B. P. Abbott *et al.* (KAGRA, LIGO Scientific, and Virgo Collaborations), Living Rev. Relativity **21**, 3 (2018).
[7] B. P. Abbott *et al.* (LIGO Scientific and Virgo Collaborations), Astrophys. J. Lett. **882**, L24 (2019).
[8] B. P. Abbott *et al.* (LIGO Scientific and Virgo Collaborations), Phys. Rev. D **100**, 104036 (2019).
[9] P. B. Graff, A. Buonanno, and B. S. Sathyaprakash, Phys. Rev. D **92**, 022002 (2015).
[10] L. London, S. Khan, E. Fauchon-Jones, C. García, M. Hannam, S. Husa, X. Jiménez-Forteza, C. Kalaghatgi, F. Ohme, and F. Pannarale, Phys. Rev. Lett. **120**, 161102 (2018).
[11] K. Chatziioannou *et al.*, Phys. Rev. D **100**, 104015 (2019).
[12] C. Kalaghatgi, M. Hannam, and V. Raymond, arXiv:1909.10010.
[13] J. Calderón Bustillo, J. A. Clark, P. Laguna, and D. Shoemaker, Phys. Rev. Lett. **121**, 191102 (2018).
[14] F. H. Shaik, J. Lange, S. E. Field, R. O'Shaughnessy, V. Varma, L. E. Kidder, H. P. Pfeiffer, and D. Wysocki, arXiv:1911.02693.
[15] T. A. Apostolatos, C. Cutler, G. J. Sussman, and K. S. Thorne, Phys. Rev. D **49**, 6274 (1994).
[16] L. E. Kidder, Phys. Rev. D **52**, 821 (1995).
[17] P. Schmidt, M. Hannam, S. Husa, and P. Ajith, Phys. Rev. D **84**, 024046 (2011).
[18] M. Boyle, R. Owen, and H. P. Pfeiffer, Phys. Rev. D **84**, 124011 (2011).
[19] R. O'Shaughnessy, J. Healy, L. London, Z. Meeks, and D. Shoemaker, Phys. Rev. D **85**, 084003 (2012).
[20] P. Schmidt, M. Hannam, and S. Husa, Phys. Rev. D **86**, 104063 (2012).
[21] L. Pekowsky, R. O'Shaughnessy, J. Healy, and D. Shoemaker, Phys. Rev. D **88**, 024040 (2013).

[22] M. Boyle, L. E. Kidder, S. Ossokine, and H. P. Pfeiffer, arXiv:1409.4431.
[23] R. O'Shaughnessy, B. Vaishnav, J. Healy, Z. Meeks, and D. Shoemaker, Phys. Rev. D **84**, 124002 (2011).
[24] S. Fairhurst, R. Green, C. Hoy, M. Hannam, and A. Muir, arXiv:1908.05707.
[25] C. Capano, Y. Pan, and A. Buonanno, Phys. Rev. D **89**, 102003 (2014).
[26] V. Varma and P. Ajith, Phys. Rev. D **96**, 124024 (2017).
[27] J. Calderón Bustillo, F. Salemi, T. Dal Canton, and K. P. Jani, Phys. Rev. D **97**, 024016 (2018).
[28] I. Harry, S. Privitera, A. Bohé, and A. Buonanno, Phys. Rev. D **94**, 024012 (2016).
[29] I. Harry, J. Calderón Bustillo, and A. Nitz, Phys. Rev. D **97**, 023004 (2018).
[30] J. Calderón Bustillo, S. Husa, A. M. Sintes, and M. Pürrer, Phys. Rev. D **93**, 084019 (2016).
[31] A. Buonanno and T. Damour, Phys. Rev. D **59**, 084006 (1999).
[32] Y. Pan, A. Buonanno, A. Taracchini, L. E. Kidder, A. H. Mroué, H. P. Pfeiffer, M. A. Scheel, and B. Szilágyi, Phys. Rev. D **89**, 084006 (2014).
[33] A. Buonanno and T. Damour, Phys. Rev. D **62**, 064015 (2000).
[34] Y. Pan, A. Buonanno, M. Boyle, L. T. Buchman, L. E. Kidder, H. P. Pfeiffer, and M. A. Scheel, Phys. Rev. D **84**, 124052 (2011).
[35] A. Taracchini *et al.*, Phys. Rev. D **89**, 061502 (2014).
[36] L. Blanchet, Living Rev. Relativity **17**, 2 (2014).
[37] M. Hannam, P. Schmidt, A. Bohé, L. Haegel, S. Husa, F. Ohme, G. Pratten, and M. Pürrer, Phys. Rev. Lett. **113**, 151101 (2014).
[38] P. Ajith *et al.*, Classical Quantum Gravity **24**, S689 (2007).
[39] L. Santamaría, F. Ohme, P. Ajith, B. Brügmann, N. Dorband, M. Hannam, S. Husa, P. Mösta, D. Pollney, C. Reisswig, E. L. Robinson, J. Seiler, and B. Krishnan, Phys. Rev. D **82**, 064016 (2010).
[40] S. Khan, S. Husa, M. Hannam, F. Ohme, M. Pürrer, X. Jiménez Forteza, and A. Bohé, Phys. Rev. D **93**, 044007 (2016).
[41] R. Cotesta, A. Buonanno, A. Bohé, A. Taracchini, I. Hinder, and S. Ossokine, Phys. Rev. D **98**, 084028 (2018).
[42] A. Bohé, L. Shao, A. Taracchini, A. Buonanno, S. Babak, I. W. Harry, I. Hinder, S. Ossokine, M. Pürrer, V. Raymond, T. Chu, H. Fong, P. Kumar, H. P. Pfeiffer, M. Boyle, D. A. Hemberger, L. E. Kidder, G. Lovelace, M. A. Scheel, and B. Szilágyi, Phys. Rev. D **95**, 044028 (2017).
[43] S. Babak, A. Taracchini, and A. Buonanno, Phys. Rev. D **95**, 024010 (2017).
[44] J. Blackman, S. E. Field, M. A. Scheel, C. R. Galley, C. D. Ott, M. Boyle, L. E. Kidder, H. P. Pfeiffer, and B. Szilágyi, Phys. Rev. D **96**, 024058 (2017).
[45] A. Nagar, S. Bernuzzi, W. Del Pozzo, G. Riemenschneider, S. Akcay, G. Carullo, P. Fleig, S. Babak, K. W. Tsang, M. Colleoni, F. Messina, G. Pratten, D. Radice, P. Rettegno, M. Agathos, E. Fauchon-Jones, M. Hannam, S. Husa, T. Dietrich, P. Cerdá-Duran, J. A. Font, F. Pannarale, P. Schmidt, and T. Damour, Phys. Rev. D **98**, 104052 (2018).
[46] A. K. Mehta, P. Tiwari, N. K. Johnson-McDaniel, C. K. Mishra, V. Varma, and P. Ajith, Phys. Rev. D **100**, 024032 (2019).
[47] V. Varma, S. E. Field, M. A. Scheel, J. Blackman, L. E. Kidder, and H. P. Pfeiffer, Phys. Rev. D **99**, 064045 (2019).
[48] D. Williams, I. S. Heng, J. Gair, J. A. Clark, and B. Khamesra, arXiv:1903.09204.
[49] Y. E. Setyawati, F. Ohme, and S. Khan, Phys. Rev. D **99**, 024010 (2019).
[50] S. Khan, K. Chatziioannou, M. Hannam, and F. Ohme, Phys. Rev. D **100**, 024059 (2019).
[51] A. Lundgren and R. O'Shaughnessy, Phys. Rev. D **89**, 044021 (2014).
[52] Z. Doctor, B. Farr, D. E. Holz, and M. Pürrer, Phys. Rev. D **96**, 123011 (2017).
[53] J. Blackman, S. E. Field, M. A. Scheel, C. R. Galley, D. A. Hemberger, P. Schmidt, and R. Smith, Phys. Rev. D **95**, 104023 (2017).
[54] V. Varma, S. E. Field, M. A. Scheel, J. Blackman, D. Gerosa, L. C. Stein, L. E. Kidder, and H. P. Pfeiffer, Phys. Rev. Research **1**, 033015 (2019).
[55] K. Chatziioannou, A. Klein, N. Yunes, and N. Cornish, Phys. Rev. D **95**, 104004 (2017).
[56] K. Chatziioannou, A. Klein, N. Cornish, and N. Yunes, Phys. Rev. Lett. **118**, 051101 (2017).
[57] https://data.black-holes.org/waveforms/index.html.
[58] Y. Pan, A. Buonanno, A. Taracchini, L. E. Kidder, A. H. Mroué, H. P. Pfeiffer, M. A. Scheel, and B. Szilágyi, Phys. Rev. D **89**, 084006 (2014).
[59] M. Vallisneri, J. Kanner, R. Williams, A. Weinstein, and B. Stephens, J. Phys. Conf. Ser. **610**, 012021 (2015).
[60] P. Schmidt, M. Hannam, S. Husa, and P. Ajith, Phys. Rev. D **84**, 024046 (2011).
[61] P. Ajith *et al.*, arXiv:0709.0093.
[62] S. Droz, D. J. Knapp, E. Poisson, and B. J. Owen, Phys. Rev. D **59**, 124016 (1999).
[63] A. H. Mroué, M. A. Scheel, B. Szilágyi, H. P. Pfeiffer, M. Boyle, D. A. Hemberger, L. E. Kidder, G. Lovelace, S. Ossokine, N. W. Taylor, A. i. e. i. f. Zenginoğlu, L. T. Buchman, T. Chu, E. Foley, M. Giesler, R. Owen, and S. A. Teukolsky, Phys. Rev. Lett. **111**, 241104 (2013).
[64] M. Boyle *et al.*, Classical Quantum Gravity **36**, 195006 (2019).
[65] P. Schmidt, I. W. Harry, and H. P. Pfeiffer, arXiv:1703.01076.
[66] https://dcc.ligo.org/LIGO-T0900288/public.
[67] https://dcc.ligo.org/LIGO-T1800044/public.
[68] S. Vitale, R. Lynch, V. Raymond, R. Sturani, J. Veitch, and P. Graff, Phys. Rev. D **95**, 064053 (2017).
[69] S. Vitale and M. Evans, Phys. Rev. D **95**, 064052 (2017).
[70] P. Kumar, J. Blackman, S. E. Field, M. Scheel, C. R. Galley, M. Boyle, L. E. Kidder, H. P. Pfeiffer, B. Szilagyi, and S. A. Teukolsky, Phys. Rev. D **99**, 124005 (2019).
[71] A. Ghosh, W. Del Pozzo, and P. Ajith, Phys. Rev. D **94**, 104070 (2016).
[72] C. Pankow, L. Sampson, L. Perri, E. Chase, S. Coughlin, M. Zevin, and V. Kalogera, Astrophys. J. **834**, 154 (2017).
[73] S. Vitale, R. Lynch, J. Veitch, V. Raymond, and R. Sturani, Phys. Rev. Lett. **112**, 251101 (2014).
[74] B. Farr *et al.*, Astrophys. J. **825**, 116 (2016).

[75] M. Pürrer, M. Hannam, and F. Ohme, Phys. Rev. D **93**, 084042 (2016).
[76] S. Stevenson, C. P. L. Berry, and I. Mandel, Mon. Not. R. Astron. Soc. **471**, 2801 (2017).
[77] J. Calderón Bustillo, P. Laguna, and D. Shoemaker, Phys. Rev. D **95**, 104038 (2017).
[78] J. Veitch *et al.*, Phys. Rev. D **91**, 042003 (2015).
[79] M. Vallisneri, Phys. Rev. D **77**, 042001 (2008).
[80] M. Purrer, M. Hannam, and F. Ohme, Phys. Rev. D **93**, 084042 (2016).
[81] E. Poisson and C. M. Will, Phys. Rev. D **52**, 848 (1995).
[82] P. Ajith, Phys. Rev. D **84**, 084037 (2011).
[83] J. D. Schnittman, Phys. Rev. D **70**, 124020 (2004).
[84] S. Husa, S. Khan, M. Hannam, M. Pürrer, F. Ohme, X. J. Forteza, and A. Bohé, Phys. Rev. D **93**, 044006 (2016).
[85] P. Schmidt, F. Ohme, and M. Hannam, Phys. Rev. D **91**, 024043 (2015).
[86] E. Payne, C. Talbot, and E. Thrane, Phys. Rev. D **100**, 123017 (2019).
[87] https://dcc.ligo.org/LIGO-P1800370/public.
[88] J. Veitch *et al.*, Phys. Rev. D **91**, 042003 (2015).
[89] T. Yoshida, H. Umeda, K. Maeda, and T. Ishii, Mon. Not. R. Astron. Soc. **457**, 351 (2016).
[90] S. Stevenson, M. Sampson, J. Powell, A. Vigna-Gómez, C. J. Neijssel, D. Szécsi, and I. Mandel, arXiv:1904.02821.
[91] K. Belczynski, A. Heger, W. Gladysz, A. J. Ruiter, S. Woosley, G. Wiktorowicz, H.-Y. Chen, T. Bulik, R. O′ Shaughnessy, D. E. Holz, C. L. Fryer, and E. Berti, Astron. Astrophys. **594**, A97 (2016).
[92] P. Marchant, M. Renzo, R. Farmer, K. M. W. Pappas, R. E. Taam, S. de Mink, and V. Kalogera, Astrophys. J. **882**. 36 (2019).
[93] S. E. Woosley, Astrophys. J. **878**, 49 (2019).
[94] C. L. Fryer, K. Belczynski, G. Wiktorowicz, M. Dominik, V. Kalogera, and D. E. Holz, Astrophys. J. **749**, 91 (2012).
[95] S. Fairhurst, R. Green, M. Hannam, and C. Hoy, arXiv:1908.00555.
[96] S. Fairhurst, R. Green, C. Hoy, M. Hannam, and A. Muir, arXiv:1908.05707.
[97] R. Farmer, M. Renzo, S. E. de Mink, P. Marchant, and S. Justham, Astrophys. J. **887**, 53 (2019).
[98] R. Smith, S. E. Field, K. Blackburn, C.-J. Haster, M. Pürrer, V. Raymond, and P. Schmidt, Phys. Rev. D **94**, 044031 (2016).
[99] S. Vinciguerra, J. Veitch, and I. Mandel, Classical Quantum Gravity **34**, 115006 (2017).
[100] C. García Quirós *et al.* (to be published).
[101] E. Hamilton *et al.* (to be published).
[102] P. Geraint *et al.* (to be published).
[103] E. Berti and A. Klein, Phys. Rev. D **90**, 064012 (2014).
[104] B. Bruegmann, J. A. Gonzalez, M. Hannam, S. Husa, and U. Sperhake, Phys. Rev. D **77**, 124047 (2008).
[105] T. Dietrich, S. Khan *et al.*, Phys. Rev. D **99**, 024029 (2019).
[106] T. Dietrich, A. Samajdar, S. Khan, N. K. McDaniel, R. Dudi, and W. Tichy, Phys. Rev. D **100**, 044003 (2019).
[107] LIGO Scientific Collaboration, LIGO Algorithm Library–LALSuite, free software (GPL) (2018).
[108] https://www.python.org/.
[109] E. Jones, T. Oliphant, P. Peterson *et al.*, SciPy: Open source scientific tools for Python (2001).
[110] J. D. Hunter, Comput. Sci. Eng. **9**, 90 (2007).
[111] A. Nitz *et al.*, Pycbc software (2018).